EUROPEAN LABORATORY FOR PARTICLE PHYSICS

CERN-EP/98-091
4 June 1998

Inclusive Production of Charged Hadrons and K^0_S Mesons in Photon-Photon Collisions

The OPAL Collaboration

Abstract

The production of charged hadrons and K^0_S mesons in the collisions of quasi-real photons has been measured using the OPAL detector at LEP. The data were taken at e^+e^- centre-of-mass energies of 161 and 172 GeV. The differential cross-sections as a function of the transverse momentum and the pseudorapidity of the charged hadrons and K^0_S mesons have been compared to the leading order Monte Carlo simulations of PHOJET and PYTHIA and to perturbative next-to-leading order (NLO) QCD calculations. The distributions have been measured in the range $10 < W < 125$ GeV of the hadronic invariant mass W. By comparing the transverse momentum distribution of charged hadrons measured in $\gamma\gamma$ interactions with γ-proton and meson-proton data we find evidence for hard photon interactions in addition to the purely hadronic photon interactions.

(submitted to European Physics Journal C)

The OPAL Collaboration

K. Ackerstaff[8], G. Alexander[23], J. Allison[16], N. Altekamp[5], K.J. Anderson[9], S. Anderson[12], S. Arcelli[2], S. Asai[24], S.F. Ashby[1], D. Axen[29], G. Azuelos[18,a], A.H. Ball[17], E. Barberio[8], R.J. Barlow[16], R. Bartoldus[3], J.R. Batley[5], S. Baumann[3], J. Bechtluft[14], T. Behnke[8], K.W. Bell[20], G. Bella[23], S. Bentvelsen[8], S. Bethke[14], S. Betts[15], O. Biebel[14], A. Biguzzi[5], S.D. Bird[16], V. Blobel[27], I.J. Bloodworth[1], M. Bobinski[10], P. Bock[11], J. Böhme[14], M. Boutemeur[34], S. Braibant[8], P. Bright-Thomas[1], R.M. Brown[20], H.J. Burckhart[8], C. Burgard[8], R. Bürgin[10], P. Capiluppi[2], R.K. Carnegie[6], A.A. Carter[13], J.R. Carter[5], C.Y. Chang[17], D.G. Charlton[1,b], D. Chrisman[4], C. Ciocca[2], P.E.L. Clarke[15], E. Clay[15], I. Cohen[23], J.E. Conboy[15], O.C. Cooke[8], C. Couyoumtzelis[13], R.L. Coxe[9], M. Cuffiani[2], S. Dado[22], G.M. Dallavalle[2], R. Davis[30], S. De Jong[12], L.A. del Pozo[4], A. de Roeck[8], K. Desch[8], B. Dienes[33,d], M.S. Dixit[7], M. Doucet[18], J. Dubbert[34], E. Duchovni[26], G. Duckeck[34], I.P. Duerdoth[16], D. Eatough[16], P.G. Estabrooks[6], E. Etzion[23], H.G. Evans[9], F. Fabbri[2], A. Fanfani[2], M. Fanti[2], A.A. Faust[30], F. Fiedler[27], M. Fierro[2], H.M. Fischer[3], I. Fleck[8], R. Folman[26], A. Fürtjes[8], D.I. Futyan[16], P. Gagnon[7], J.W. Gary[4], J. Gascon[18], S.M. Gascon-Shotkin[17], C. Geich-Gimbel[3], T. Geralis[20], G. Giacomelli[2], P. Giacomelli[2], V. Gibson[5], W.R. Gibson[13], D.M. Gingrich[30,a], D. Glenzinski[9], J. Goldberg[22], W. Gorn[4], C. Grandi[2], E. Gross[26], J. Grunhaus[23], M. Gruwé[27], G.G. Hanson[12], M. Hansroul[8], M. Hapke[13], C.K. Hargrove[7], C. Hartmann[3], M. Hauschild[8], C.M. Hawkes[5], R. Hawkings[27], R.J. Hemingway[6], M. Herndon[17], G. Herten[10], R.D. Heuer[8], M.D. Hildreth[8], J.C. Hill[5], S.J. Hillier[1], P.R. Hobson[25], A. Hocker[9], R.J. Homer[1], A.K. Honma[28,a], D. Horváth[32,c], K.R. Hossain[30], R. Howard[29], P. Hüntemeyer[27], P. Igo-Kemenes[11], D.C. Imrie[25], K. Ishii[24], F.R. Jacob[20], A. Jawahery[17], H. Jeremie[18], M. Jimack[1], A. Joly[18], C.R. Jones[5], P. Jovanovic[1], T.R. Junk[8], D. Karlen[6], V. Kartvelishvili[16], K. Kawagoe[24], T. Kawamoto[24], P.I. Kayal[30], R.K. Keeler[28], R.G. Kellogg[17], B.W. Kennedy[20], A. Klier[26], S. Kluth[8], T. Kobayashi[24], M. Kobel[3,e], D.S. Koetke[6], T.P. Kokott[3], M. Kolrep[10], S. Komamiya[24], R.V. Kowalewski[28], T. Kress[11], P. Krieger[6], J. von Krogh[11], P. Kyberd[13], G.D. Lafferty[16], D. Lanske[14], J. Lauber[15], S.R. Lautenschlager[31], I. Lawson[28], J.G. Layter[4], D. Lazic[22], A.M. Lee[31], E. Lefebvre[18], D. Lellouch[26], J. Letts[12], L. Levinson[26], R. Liebisch[11], B. List[8], C. Littlewood[5], A.W. Lloyd[1], S.L. Lloyd[13], F.K. Loebinger[16], G.D. Long[28], M.J. Losty[7], J. Ludwig[10], D. Lui[12], A. Macchiolo[2], A. Macpherson[30], M. Mannelli[8], S. Marcellini[2], C. Markopoulos[13], A.J. Martin[13], J.P. Martin[18], G. Martinez[17], T. Mashimo[24], P. Mättig[26], W.J. McDonald[30], J. McKenna[29], E.A. Mckigney[15], T.J. McMahon[1], R.A. McPherson[28], F. Meijers[8], S. Menke[3], F.S. Merritt[9], H. Mes[7], J. Meyer[27], A. Michelini[2], S. Mihara[24], G. Mikenberg[26], D.J. Miller[15], R. Mir[26], W. Mohr[10], A. Montanari[2], T. Mori[24], K. Nagai[26], I. Nakamura[24], H.A. Neal[12], B. Nellen[3], R. Nisius[8], S.W. O'Neale[1], F.G. Oakham[7], F. Odorici[2], H.O. Ogren[12], M.J. Oreglia[9], S. Orito[24], J. Pálinkás[33,d], G. Pásztor[32], J.R. Pater[16], G.N. Patrick[20], J. Patt[10], R. Perez-Ochoa[8], S. Petzold[27], P. Pfeifenschneider[14], J.E. Pilcher[9], J. Pinfold[30], D.E. Plane[8], P. Poffenberger[28], B. Poli[2], J. Polok[8], M. Przybycień[8], C. Rembser[8], H. Rick[8], S. Robertson[28], S.A. Robins[22], N. Rodning[30], J.M. Roney[28], K. Roscoe[16], A.M. Rossi[2], Y. Rozen[22], K. Runge[10], O. Runolfsson[8], D.R. Rust[12], K. Sachs[10], T. Saeki[24], O. Sahr[34], W.M. Sang[25], E.K.G. Sarkisyan[23], C. Sbarra[29], A.D. Schaile[34], O. Schaile[34], F. Scharf[3], P. Scharff-Hansen[8], J. Schieck[11], B. Schmitt[8], S. Schmitt[11], A. Schöning[8], T. Schorner[34], M. Schröder[8], M. Schumacher[3], C. Schwick[8], W.G. Scott[20], R. Seuster[14], T.G. Shears[8], B.C. Shen[4], C.H. Shepherd-Themistocleous[8], P. Sherwood[15], G.P. Siroli[2], A. Sittler[27], A. Skuja[17], A.M. Smith[8], G.A. Snow[17], R. Sobie[28], S. Söldner-Rembold[10], M. Sproston[20], A. Stahl[3], K. Stephens[16], J. Steuerer[27], K. Stoll[10],

D. Strom[19], R. Ströhmer[34], R. Tafirout[18], S.D. Talbot[1], S. Tanaka[24], P. Taras[18], S. Tarem[22], R. Teuscher[8], M. Thiergen[10], M.A. Thomson[8], E. von Törne[3], E. Torrence[8], S. Towers[6], I. Trigger[18], Z. Trócsányi[33], E. Tsur[23], A.S. Turcot[9], M.F. Turner-Watson[8], R. Van Kooten[12], P. Vannerem[10], M. Verzocchi[10], P. Vikas[18], H. Voss[3], F. Wäckerle[10], A. Wagner[27], C.P. Ward[5], D.R. Ward[5], P.M. Watkins[1], A.T. Watson[1], N.K. Watson[1], P.S. Wells[8], N. Wermes[3], J.S. White[28], T. Wiesler[10], G.W. Wilson[14], J.A. Wilson[1], T.R. Wyatt[16], S. Yamashita[24], G. Yekutieli[26], V. Zacek[18], D. Zer-Zion[8]

[1]School of Physics and Astronomy, University of Birmingham, Birmingham B15 2TT, UK
[2]Dipartimento di Fisica dell' Università di Bologna and INFN, I-40126 Bologna, Italy
[3]Physikalisches Institut, Universität Bonn, D-53115 Bonn, Germany
[4]Department of Physics, University of California, Riverside CA 92521, USA
[5]Cavendish Laboratory, Cambridge CB3 0HE, UK
[6]Ottawa-Carleton Institute for Physics, Department of Physics, Carleton University, Ottawa, Ontario K1S 5B6, Canada
[7]Centre for Research in Particle Physics, Carleton University, Ottawa, Ontario K1S 5B6, Canada
[8]CERN, European Organisation for Particle Physics, CH-1211 Geneva 23, Switzerland
[9]Enrico Fermi Institute and Department of Physics, University of Chicago, Chicago IL 60637, USA
[10]Fakultät für Physik, Albert-Ludwigs-Universität, D-79104 Freiburg, Germany
[11]Physikalisches Institut, Universität Heidelberg, D-69120 Heidelberg, Germany
[12]Indiana University, Department of Physics, Swain Hall West 117, Bloomington IN 47405, USA
[13]Queen Mary and Westfield College, University of London, London E1 4NS, UK
[14]Technische Hochschule Aachen, III Physikalisches Institut, Sommerfeldstrasse 26-28, D-52056 Aachen, Germany
[15]University College London, London WC1E 6BT, UK
[16]Department of Physics, Schuster Laboratory, The University, Manchester M13 9PL, UK
[17]Department of Physics, University of Maryland, College Park, MD 20742, USA
[18]Laboratoire de Physique Nucléaire, Université de Montréal, Montréal, Quebec H3C 3J7, Canada
[19]University of Oregon, Department of Physics, Eugene OR 97403, USA
[20]Rutherford Appleton Laboratory, Chilton, Didcot, Oxfordshire OX11 0QX, UK
[22]Department of Physics, Technion-Israel Institute of Technology, Haifa 32000, Israel
[23]Department of Physics and Astronomy, Tel Aviv University, Tel Aviv 69978, Israel
[24]International Centre for Elementary Particle Physics and Department of Physics, University of Tokyo, Tokyo 113, and Kobe University, Kobe 657, Japan
[25]Institute of Physical and Environmental Sciences, Brunel University, Uxbridge, Middlesex UB8 3PH, UK
[26]Particle Physics Department, Weizmann Institute of Science, Rehovot 76100, Israel
[27]Universität Hamburg/DESY, II Institut für Experimental Physik, Notkestrasse 85, D-22607 Hamburg, Germany
[28]University of Victoria, Department of Physics, P O Box 3055, Victoria BC V8W 3P6, Canada
[29]University of British Columbia, Department of Physics, Vancouver BC V6T 1Z1, Canada
[30]University of Alberta, Department of Physics, Edmonton AB T6G 2J1, Canada

[31]Duke University, Dept of Physics, Durham, NC 27708-0305, USA
[32]Research Institute for Particle and Nuclear Physics, H-1525 Budapest, P O Box 49, Hungary
[33]Institute of Nuclear Research, H-4001 Debrecen, P O Box 51, Hungary
[34]Ludwigs-Maximilians-Universität München, Sektion Physik, Am Coulombwall 1, D-85748 Garching, Germany

[a] and at TRIUMF, Vancouver, Canada V6T 2A3
[b] and Royal Society University Research Fellow
[c] and Institute of Nuclear Research, Debrecen, Hungary
[d] and Department of Experimental Physics, Lajos Kossuth University, Debrecen, Hungary
[e] on leave of absence from the University of Freiburg

1 Introduction

Inclusive hadron production in collisions of quasi-real photons can be used to study the structure of photon interactions complementing similar studies of jet production in $\gamma\gamma$ collisions [1]. The photons are radiated by the beam electrons[1] carrying only small negative squared four-momenta Q^2. They can therefore be considered to be quasi-real ($Q^2 \approx 0$) if the electrons are scattered at very small angles where they are not detected. For the "anti-tagged" event sample, events are rejected if one or both scattered electrons have been detected.

The interactions of the photons can be modelled by assuming that each photon can either interact directly or appear resolved through its fluctuations into hadronic states. In leading order Quantum Chromodynamics (QCD) this model leads to three different event classes for the $\gamma\gamma$ interactions: direct, single-resolved and double-resolved. In resolved events partons (quarks or gluons) from the hadronic fluctuation of the photon take part in the hard interaction. The probability to find a parton in the photon carrying a certain momentum fraction of the photon is parametrised by parton density functions.

We measure differential production cross-sections as a function of the transverse momentum and the pseudorapidity of charged hadrons and neutral K^0_S mesons. Since the distributions are fully corrected for losses due to event and track selection cuts, the acceptance and the resolution of the detector, they are directly comparable to leading order Monte Carlo models and to next-to-leading order (NLO) perturbative QCD calculations by Binnewies, Kniehl and Kramer [2]. Until now, transverse momentum distributions of charged hadrons have only been measured for single-tagged events by TASSO [3] and MARK II [4] at an average $\langle Q^2 \rangle$ of 0.35 GeV^2 and 0.5 GeV^2, respectively. We present the first measurement in anti-tagged collisions of quasi-real photons. Furthermore, the transverse momentum distributions in $\gamma\gamma$ interactions are expected to have a harder component than in photon-proton or meson-proton interactions due to the direct photon interactions. This will be demonstrated by comparing our data to the photo- and hadroproduction data measured by WA69 [5].

[1]Positrons are also referred to as electrons

At large transverse momenta (after crossing the charm threshold) the production of K^0_S mesons in photon-photon collisions is sensitive to the direct production of primary charm quarks in addition to the production of primary strange quarks, since the photon couples to the quark charge. K^0_S production in anti-tagged $\gamma\gamma$ collisions has previously been measured by TOPAZ [6] and in single-tagged events by MARK II [4].

In this paper, charged hadron and K^0_S production are studied using the full data sample taken in 1996 at e^+e^- centre-of-mass energies of 161 and 172 GeV corresponding to an integrated luminosity of about 20 pb^{-1}.

2 The OPAL detector

A detailed description of the OPAL detector can be found in Ref. [7], and therefore only a brief account of the main features relevant to the present analysis will be given here.

The central tracking system is located inside a solenoidal magnet which provides a uniform axial magnetic field of 0.435 T along the beam axis[2]. The detection efficiency for charged particles is close to 100 % within the polar angle range $|\cos\theta| < 0.92$. The magnet is surrounded in the barrel region ($|\cos\theta| < 0.82$) by a lead glass electromagnetic calorimeter (ECAL) and a hadronic sampling calorimeter (HCAL). Outside the HCAL, the detector is surrounded by muon chambers. There are similar layers of detectors in the endcaps ($0.81 < |\cos\theta| < 0.98$). The small angle region from 47 to 140 mrad around the beam pipe on both sides of the interaction point is covered by the forward calorimeters (FD) and the region from 25 to 59 mrad by the silicon tungsten luminometers (SW). From 1996 onwards, including the data presented in this paper, the lower boundary of the acceptance has been increased to 33 mrad following the installation of a low angle shield to protect the central detector against possible synchrotron radiation.

Starting with the innermost components, the tracking system consists of a high precision silicon microvertex detector, a vertex drift chamber, a large volume jet chamber with 159 layers of axial anode wires and a set of z chambers measuring the track coordinates along the beam direction. The transverse momenta p_T of tracks are measured with a precision parametrised by $\sigma_{p_T}/p_T = \sqrt{0.02^2 + (0.0015 \cdot p_T)^2}$ (p_T in GeV/c) in the central region. In this paper "transverse" is always defined with respect to the z axis. The jet chamber also provides measurements of the energy loss, dE/dx, which are used for particle identification [7].

The barrel and endcap sections of the ECAL are both constructed from lead glass blocks with a depth of 24.6 radiation lengths in the barrel region and more than 22 radiation lengths in the endcaps. The FD consist of cylindrical lead-scintillator calorimeters with a depth of 24 radiation lengths divided azimuthally into 16 segments. The electromagnetic energy resolution is about $18\%/\sqrt{E}$, where E is in GeV. The SW detectors [8] consist of 19 layers of silicon detectors and 18 layers of tungsten, corresponding to a total of 22 radiation lengths. Each silicon layer consists of 16 wedge shaped silicon detectors. The electromagnetic energy resolution is about $25\%/\sqrt{E}$ (E in GeV).

[2] In the OPAL coordinate system the z axis points in the direction of the e^- beam. The polar angle θ, the azimuthal angle ϕ and the radius r denote the usual spherical coordinates.

3 Kinematics and Monte Carlo simulation

The properties of the two interacting photons ($i = 1, 2$) are described by their negative four-momentum transfers Q_i^2. Each Q_i^2 is related to the electron scattering angle θ_i' relative to the beam direction by

$$Q_i^2 = -(p_i - p_i')^2 \approx 2E_i E_i'(1 - \cos\theta_i'), \tag{1}$$

where p_i and p_i' are the four-momenta of the beam electrons and the scattered electrons, respectively, and E_i and E_i' are their energies. Events with detected scattered electrons (single-tagged or double-tagged events) are excluded from the analysis. This anti-tagging condition is met when the scattering angle θ' of the electron is less than 33 mrad between the beam axis and the inner edge of the SW detector. It defines an effective upper limit, $Q^2_{\max}$, on the values of Q_i^2 for both photons. The hadronic final state is described by its invariant mass W. The spectrum of photons with an energy fraction y of the electron beam may be obtained by the Equivalent Photon Approximation (EPA) [9]:

$$f_{\gamma/\mathrm{e}}(y) = \frac{\alpha}{2\pi}\left(\frac{1+(1-y)^2}{y}\log\frac{Q^2_{\max}}{Q^2_{\min}} - 2m_{\mathrm{e}}^2 y\left(\frac{1}{Q^2_{\min}} - \frac{1}{Q^2_{\max}}\right)\right), \tag{2}$$

with α being the electromagnetic coupling constant. The minimum kinematically allowed negative squared four-momentum transfer $Q^2_{\min}$ is determined by the electron mass m_{e}:

$$Q^2_{\min} = \frac{m_{\mathrm{e}}^2 y^2}{1-y}. \tag{3}$$

The Monte Carlo generators PYTHIA [10] and PHOJET [11] have been used to simulate quasi-real photon-photon interactions. More details about the event generation can be found in Ref. [1]. All possible hard interactions relevant to photon-photon interactions are included. The fragmentation is handled by JETSET [10]. PYTHIA uses the SaS-1D parametrisation [12] for the parton densities of the photon and PHOJET uses the GRV parametrisation [13]. An approximation is used for the processes with primary charm quarks, i.e. where the charm quark is produced in the hard interaction. These processes are simulated using the matrix elements for light quarks. Subsequently the charm quarks are put on the mass-shell.

4 Event selection and background

The production of charged hadrons and $\mathrm{K}^0_{\mathrm{S}}$ mesons was studied using the data taken at $\mathrm{e^+e^-}$ centre-of-mass energies, $\sqrt{s}_{\mathrm{ee}}$, of 161 and 172 GeV with an integrated luminosity of about 9.9 pb^{-1} and 10.0 pb^{-1}, respectively. Photon-photon events are selected with the following set of cuts:

- The sum of all energy deposits in the ECAL and the HCAL has to be less than 45 GeV.
- The visible invariant hadronic mass, W_{ECAL}, calculated from the position and the energy of the clusters measured in the ECAL, has to be greater than 3 GeV.

- The missing transverse energy of the event measured in the ECAL and the forward calorimeters has to be less than 5 GeV.

- At least 3 tracks must have been found in the tracking chambers. A track is required to have a minimum transverse momentum of 120 MeV/c, at least 20 hits in the central jet chamber, and the innermost hit of the track must be within a radius of 60 cm with respect to the z axis. The distance of the point of closest approach to the origin in the rϕ plane must be less than 30 cm in the z direction and less than 2 cm in the $r\phi$ plane. Tracks with a momentum error larger than the momentum itself are rejected if they have fewer than 80 hits. The number of measured hits in the jet chamber must be more than half of the number of possible hits. The number of possible hits is calculated from the polar angle $\cos\theta$ of the track, assuming that the track has no curvature.

- To remove events with scattered electrons in the FD or SW, the total energy measured in the FD has to be less than 50 GeV and the total energy measured in the SW has to be less than 35 GeV. These cuts also reduce contamination from multihadronic events with their thrust axis close to the beam direction.

- To reduce the background due to beam-gas and beam-wall interactions, $|\langle z_0\rangle|$ must be smaller than 10 cm where $\langle z_0\rangle$ is the error-weighted average of the track's z coordinates at the point of closest approach to the origin in the $r\phi$ plane. Beam-wall events with a vertex in the beam-pipe are rejected by requiring the radial position of the primary vertex in the $r\phi$ plane to be less than 3 cm.

After all cuts 56732 events remain.

All relevant background processes apart from beam-gas and beam-wall events were studied using Monte Carlo generators. Multihadronic events ($e^+e^- \to q\overline{q}(\gamma)$) were simulated with PYTHIA 5.722 [10]. KORALZ 4.02 [14] was used to generate the process $e^+e^- \to \tau^+\tau^-(\gamma)$ and BHWIDE [15] to generate the Bhabha process $e^+e^- \to e^+e^-(\gamma)$. Processes with four fermions in the final state, including W pair production, were simulated with grc4f [16], EXCALIBUR [17], VERMASEREN [18] and FERMISV [19]. All signal and background Monte Carlo samples were generated with a full simulation of the OPAL detector [20]. They were analysed using the same reconstruction algorithms as for the data. The main background processes are multi-hadronic e^+e^- annihilation events and $e^+e^- \to e^+e^-\tau^+\tau^-$ events. Other background processes are found to be negligible. The multihadronic background is mainly reduced by the cut on the sum of the energy measured by the HCAL and the ECAL and by the cut on the missing transverse energy. The background from all these processes after the selection cuts amounts to less than 1%.

The cut on the energy in SW and FD rejects photon-photon events with electrons scattered at angles θ' larger than 33 mrad and with an energy greater than 35 GeV in the SW or greater than 50 GeV in the FD. From the Monte Carlo, the rate of events with $\theta' > 33$ mrad and energies less than 50 GeV is estimated to be negligible. The effective anti-tagging condition is therefore $\theta' < 33$ mrad.

5 Analysis

5.1 Correction procedure

The measured transverse momentum and pseudorapidity distributions of the charged hadrons and the K^0_S mesons have to be corrected for losses due to the event and track selection cuts, for the acceptance and for the resolution of the detector. This is done with Monte Carlo events which were generated with PYTHIA 5.722 and PHOJET 1.05c. The data are corrected by multiplying the experimental distribution, e.g. of the transverse momentum p_T, with correction factors which are calculated as the bin-by-bin ratio of the generated and the reconstructed Monte Carlo distributions:

$$\left(\frac{d\sigma}{dp_T}\right)_{\text{corrected}} = \frac{\left(\frac{d\sigma}{dp_T}\right)^{\text{MC}}_{\text{generated}}}{\left(\frac{d\sigma}{dp_T}\right)^{\text{MC}}_{\text{reconstructed}}} \left(\frac{d\sigma}{dp_T}\right)_{\text{measured}} . \quad (4)$$

As a correction factor the mean value from PYTHIA and PHOJET is used. The distributions of the pseudorapidity $\eta = -\ln\tan(\theta/2)$ are corrected in the same way. This method only yields reliable results if the migration between bins due to the finite resolution is small. The bins of the p_T and $|\eta|$ distributions have therefore been chosen to be significantly larger than the resolution expected from the Monte Carlo simulation. The average transverse momentum, $\langle p_T \rangle$, and the average pseudorapidity, $\langle |\eta| \rangle$, in each bin is calculated directly from the data, since detector corrections are small compared to the statistical errors.

The visible invariant mass, W_{vis}, is determined from all tracks and calorimeter clusters, including the FD and the SW detectors. An algorithm is applied to avoid double-counting of particle momenta in the central tracking system and the calorimeters [1]. All distributions are shown for $10 < W < 125$ GeV where W is the hadronic invariant mass corrected for detector effects. To minimize migration effects when using Eq. 4 for the detector correction, the bins in W must be larger than the experimental resolution and the average reconstructed hadronic invariant mass, $\langle W_{\text{rec}} \rangle$, should be approximately equal to the average generated hadronic invariant mass, $\langle W_{\text{gen}} \rangle$. The average $\langle W_{\text{vis}} \rangle$ and the resolution on W_{vis} as a function of the generated hadronic invariant mass W_{gen} are therefore shown in Fig. 1a, where the vertical bars show the standard deviation (resolution) in each bin. The average $\langle W_{\text{gen}} \rangle$ as a function of W_{vis} is plotted in Fig. 1b, where the vertical bars give the error on the mean. This plot is used to determine a correction function so that $\langle W_{\text{gen}} \rangle / W_{\text{rec}} \approx 1$. The value of W_{vis} measured in the detector is on average significantly smaller than W_{gen}. The relation between W_{gen} and W_{vis} shown in Fig. 1b is almost independent of the beam energy and the Monte Carlo generator used. A single polynomial is therefore used to calculate W_{rec} from W_{vis}. The polynomial is obtained from the fit shown in Fig. 1b. It is applied to the data and the Monte Carlo.

The efficiency to reconstruct photon-photon events in the detector, estimated by the Monte Carlo, is greater than 20% for $W_{\text{gen}} > 10$ GeV and greater than 60% for $W_{\text{gen}} > 50$ GeV. The trigger efficiency is defined as the ratio of the number of selected and triggered events to the number of selected events. It was studied using data samples which were obtained using nearly independent sets of triggers. On average the trigger efficiency for the lowest W range, $10 < W < 30$ GeV, is greater than 97% and it approaches 100% for larger values of W. Only

lower limits on the trigger efficiency can be determined with this method and therefore no correction factor is applied.

5.2 Charged hadron production

For the charged hadron analysis only particles with a proper lifetime $\tau > 0.3$ ns are used to define the primary charged hadronic multiplicity in the Monte Carlo. The primary charged hadrons originate either directly from the primary interaction or from the decay of particles with a lifetime $\tau < 0.3$ ns including Λ and $\mathrm{K^0_S}$ decay products. The track selection criteria are defined as in Section 4. In order to avoid regions where the detector has little or no acceptance, all measurements of charged hadrons were restricted to the range $|\eta| < 1.5$ ($|\cos\theta| \lesssim 0.9$). In this range, the resolution on p_T is given by $\sigma_{p_\mathrm{T}}/p_\mathrm{T} \approx 0.02$ (see Section 2) and the resolution on η by $\sigma_\eta \approx 0.02$. For the p_T distribution in the range $10 < W < 125$ GeV the correction factors as defined in Eq. 4 decrease from about 1.7 for $p_\mathrm{T} > 120$ MeV/c to about $1.1 - 1.4$ for $p_\mathrm{T} > 2$ GeV/c. The correction factor of about 1.6 for the η distribution is nearly constant for $|\eta| < 1.5$. The PHOJET and PYTHIA correction factors differ by about $3 - 10$ %.

5.3 $\mathrm{K^0_S}$ production

The $\mathrm{K^0_S}$ mesons are reconstructed using the decay channel $\mathrm{K^0_S} \to \pi^+\pi^-$ which has a branching ratio of about 69% [21]. The reconstruction procedure is similar to the procedure described in Ref. [22]. It has been optimised to increase the efficiency for finding $\mathrm{K^0_S}$ mesons in photon-photon events. Tracks of opposite charge are paired together. In addition to other quality cuts the tracks must have a minimum transverse momentum of 120 MeV/c and at least 20 jet chamber hits. The intersection of the tracks in the $r\phi$ plane is considered as a secondary vertex candidate if it satisfies the following criteria:

- the radial distance between primary vertex and the intersection point must be greater than 0.5 cm and less than 150 cm. For events with at least 6 tracks the primary vertex is fitted and for events with less than 6 tracks the beam spot reconstructed from tracks collected from many consecutive $\mathrm{e^+e^-}$ events during a LEP fill is taken as primary vertex [23].
- the difference between the radial coordinate of the secondary vertex and the radial coordinate of the first jet-chamber hit associated with either of the two tracks has to be less than 10 cm;
- the radial coordinate of the tracks at the point of closest approach to the primary vertex has to be greater than 0.2 cm;
- the angle between the direction of flight from primary to secondary vertex and the combined momentum vector of the two tracks at the intersection point has to be less than 5°.

In addition, a fit was performed for track pairs passing all these cuts, constraining them to originate from a common vertex. A correction procedure was used to compensate for the

energy loss of the pions in the inactive material of the detector. All secondary vertices satisfying $|M(\pi^+\pi^-) - 0.4977\ \mathrm{GeV}/c^2| < 0.02\ \mathrm{GeV}/c^2$ are considered to be K^0_S decay vertices, where the mass M is calculated assuming that both tracks are pions. Finally, the residual background is reduced by requiring at least 20 $\mathrm{d}E/\mathrm{d}x$ hits. The two tracks are identified as pions if the $\mathrm{d}E/\mathrm{d}x$ probability for the pion hypothesis, that is the probability that the specific ionisation energy loss in the jet chamber ($\mathrm{d}E/\mathrm{d}x$) is compatible with that expected for a pion, exceeds 5%.

In Fig. 2 the $\pi^+\pi^-$ invariant mass M is shown for all identified secondary vertices in the selected events before and after applying the $\mathrm{d}E/\mathrm{d}x$ cuts. After all cuts the reconstruction efficiency for $\mathrm{K}^0_\mathrm{S} \to \pi^+\pi^-$ decays is about 35.5% and the purity is about 95.5% for $p_\mathrm{T}(\mathrm{K}^0_\mathrm{S}) > 1\ \mathrm{GeV}/c$, $|\eta(\mathrm{K}^0_\mathrm{S})| < 1.5$ and $10 < W < 125$ GeV.

6 Systematic errors

The following systematic errors, common to the charged hadron and K^0_S measurements, are taken into account:

- The correction factors are obtained using PHOJET and PYTHIA, separately. The resulting distributions are averaged to get the final result. The differences between the two distributions are used to define the systematic error.
- The lower limit on the trigger efficiency is taken into account by an additional systematic error of 3% on the cross-section in the range $10 < W < 30$ GeV.
- Systematic errors due to the modelling of the detector resolution for the measurement of tracks were found to be negligibly small in comparison to the other errors. The systematic error due to the uncertainty in the energy scale of the electromagnetic calorimeter was estimated by varying the reconstructed ECAL energy in the Monte Carlo by $\pm 5\%$.
- The limited statistics of the Monte Carlo samples, especially at large transverse momenta p_T, is also included in the systematic error.
- The systematic error of the luminosity measurement is negligible compared to the other systematic errors.

The systematic error of the Monte Carlo modelling and of the ECAL energy scale and, for the low W region, the error from the trigger efficiency contribute about equally to the total systematic error. In the K^0_S reconstruction additional systematic errors were studied by varying the parameters of the secondary vertex finder and the $\mathrm{d}E/\mathrm{d}x$ cuts. The full difference between the results is used to estimate the contribution to the total systematic error from the K^0_S reconstruction, the Monte Carlo model dependence and the ECAL energy scale. The systematic error affecting the K^0_S reconstruction and the error from comparing the PHOJET and PYTHIA correction factors are of similar magnitude. The total systematic error was obtained by adding all systematic errors in quadrature. The total systematic errors are highly correlated from bin to bin.

7 Results

The differential inclusive cross-section $\mathrm{d}\sigma/\mathrm{d}p_\mathrm{T}$ for charged hadrons in the region $|\eta| < 1.5$ is shown in Fig. 3 for different corrected W ranges together with the statistical and systematical errors. The corrected cross-sections are given in Tables 1 and 2.

The measured differential cross-sections are compared to NLO calculations by Binnewies, Kniehl and Kramer [2]. The cross-sections are calculated using the QCD partonic cross-sections to NLO for direct, single- and double-resolved processes. The hadronic cross-section is a convolution of the Weizsäcker-Williams effective photon distribution, the parton distribution functions and the fragmentation functions of Ref. [24] which are obtained from a fit to $\mathrm{e^+e^-}$ data from TPC and ALEPH. The NLO GRV parametrisation of the parton densities of the photon [13] is used with $\Lambda^{(5)}_{\overline{\mathrm{MS}}} = 131$ MeV and $m_\mathrm{c} = 1.5$ GeV/c^2. The renormalization and factorization scales in the calculation are set equal to ξp_T with $\xi = 1$. The change in slope around $p_\mathrm{T} = 3$ GeV/c in the NLO calculation is due to the charm threshold, below which the charm distribution in the resolved photon and the charm fragmentation functions are set to zero.

The cross-section calculation was repeated for the kinematic conditions of the data presented here at an average $\mathrm{e^+e^-}$ centre-of-mass energy $\sqrt{s}_\mathrm{ee} = 166.5$ GeV and for scattering angles $\theta' < 33$ mrad. For the differential cross-section $\mathrm{d}\sigma/\mathrm{d}p_\mathrm{T}$ a minimum p_T of 1 GeV/c is required to ensure the validity of the perturbative QCD calculation. For the same reason the differential cross-section $\mathrm{d}\sigma/\mathrm{d}|\eta|$ is restricted to the region $p_\mathrm{T} > 1.5$ GeV/c. The scale dependence of the NLO calculation was studied by setting $\xi = 0.5$ and 2. This leads to a variation of the cross-section of about 30% at $p_\mathrm{T} = 1$ GeV/c and of about 10% for $p_\mathrm{T} > 5$ GeV/c. The NLO calculations lie significantly below the data for $W < 30$ GeV for $\mathrm{d}\sigma/\mathrm{d}p_\mathrm{T}$ and $\mathrm{d}\sigma/\mathrm{d}|\eta|$. The agreement with the data improves in the higher W bins. The NLO calculation is shown separately for double-resolved, single-resolved and direct interactions. At large p_T the direct interactions dominate. It should be noted that these classifications are scale dependent in NLO.

The p_T distribution for $10 < W < 30$ GeV is compared in Fig. 4 to p_T distributions in γp and hp (h= π,K) interactions measured by the experiment WA69 [5]. The hp data are weighted by WA69 in such a way that they contain 60% πp and 40% Kp data to match the expected mixture of non-strange and strange quarks in the photon beam of the γp data. The WA69 data is normalised to the $\gamma\gamma$ data in the low p_T region at $p_\mathrm{T} \approx 200$ MeV/c using the same factor for the hp and the γp data. The p_T distribution of WA69 has been measured in the Feynman-x range $0.0 < x_\mathrm{F} < 1.0$. The hadronic invariant mass of the hp data is $W = 16$ GeV and the average $\langle W \rangle$ is of similar size for the γp data. In the $\gamma\gamma$ Monte Carlo the average $\langle W \rangle$ is about 17 GeV in the range $10 < W < 30$ GeV, i.e. the average values of W in the different data samples are approximately the same. Whereas only a small increase is observed in the γp data compared to the πp and Kπ data at large p_T, there is a significant increase of the relative rate in the range $p_\mathrm{T} > 2$ GeV/c for $\gamma\gamma$ interactions due to the direct process. A clear deviation is seen at large p_T from the exponential fall-off expected for purely hadronic interactions.

The differential cross-section $\mathrm{d}\sigma/\mathrm{d}|\eta|$ is compared to the predictions of the Monte Carlo generators PHOJET 1.10 and PYTHIA 5.722 in Fig. 5 taking into account the anti-tagging condition $\theta' < 33$ mrad. In PHOJET the Q^2 suppression of the total $\gamma\gamma$ cross-section is parametrised using Generalised Vector Meson Dominance (GVMD) and a model for the change of soft hadron production and diffraction with increasing photon virtuality Q^2 is also included.

The photon-photon mode of PYTHIA only simulates the interactions of real photons with $Q^2 = 0$. The virtuality of the photons defined by Q^2 enters only through the equivalent photon approximation in the generation of the photon energy spectrum, but the electrons are scattered at zero angle. This model is not expected to be correct for larger values of Q^2. We have therefore simulated events with $Q^2 < 1$ GeV^2 with the photon-photon mode of PYTHIA and events with $Q^2 > 1$ GeV^2 and $\theta' < 33$ mrad with the electron-photon mode of PYTHIA.

The differential cross-section $\mathrm{d}\sigma/\mathrm{d}|\eta|$ shown in Fig. 5 is nearly independent of $|\eta|$ in the measured range. The $|\eta|$ distribution is reasonably well described by PYTHIA and PHOJET for $p_{\mathrm{T}} > 120$ MeV/c, apart from the high W region where PHOJET appears to be below the data. For transverse momenta $p_{\mathrm{T}} > 1.5$ GeV/c (Fig. 6) both Monte Carlo models underestimate the data significantly. The same behaviour is observed for the NLO calculation at low W, but the agreement of the NLO calculation with the data improves in the high W bins. The corrected cross-sections are given in Tables 3 and 4.

The differential inclusive cross-sections $\mathrm{d}\sigma/\mathrm{d}p_{\mathrm{T}}$ and $\mathrm{d}\sigma/\mathrm{d}|\eta|$ have been measured for $\mathrm{K}^0_{\mathrm{S}}$ mesons with $p_{\mathrm{T}}(\mathrm{K}^0_{\mathrm{S}}) > 1$ GeV/c and $|\eta(\mathrm{K}^0_{\mathrm{S}})| < 1.5$. The p_{T} and η dependent cross-sections are presented in the W range $10 < W < 125$ GeV (Fig. 7 and Tables 5–6). In addition the p_{T} distribution is shown for two separate W ranges (Fig. 8 and Table 7). The results are compared to PHOJET and PYTHIA. Based on the PYTHIA simulation using SaS-1D, about half of the $\mathrm{K}^0_{\mathrm{S}}$ are expected to be produced from charm quarks at large p_{T} where direct processes are dominant. Both Monte Carlo models significantly underestimate the $\mathrm{K}^0_{\mathrm{S}}$ production cross-section in the low p_{T} region where most $\mathrm{K}^0_{\mathrm{S}}$ are expected to originate from primary strange quarks. The distributions are reasonably well described by the NLO calculations which use the $\mathrm{K}^0_{\mathrm{S}}$ fragmentation function fitted to MARK II [25] and ALEPH [26] data in Ref. [27]. The change in slope between $p_{\mathrm{T}} = 2$ and $p_{\mathrm{T}} = 3$ GeV/c in the NLO calculation is again due to the charm threshold. The variation of the calculated cross-section as a function of p_{T} for different choices of scales, $\xi = 0.5$ and 2, is largest around the charm threshold, about $30 - 40\%$, and $10 - 20\%$ elsewhere.

8 Conclusions

We present measurements of differential cross-sections as a function of transverse momentum and pseudorapidity for charged hadrons and $\mathrm{K}^0_{\mathrm{S}}$ mesons produced in photon-photon collisions at LEP. The data were taken at $\mathrm{e^+e^-}$ centre-of-mass energies of 161 and 172 GeV.

The differential cross-section $\mathrm{d}\sigma/\mathrm{d}p_{\mathrm{T}}$ for charged hadrons is compared to NLO calculations. In the range $10 < W < 30$ GeV more charged hadrons are found at large p_{T} than predicted. Good agreement between the NLO calculation and the data is found in the highest W range, $55 < W < 125$ GeV. The Monte Carlo models PYTHIA and PHOJET both underestimate the cross-section for tracks with $p_{\mathrm{T}} > 1.5$ GeV and $|\eta| < 1.5$ in all W ranges. The shape of the differential cross-section $\mathrm{d}\sigma/\mathrm{d}|\eta|$ is well reproduced by the NLO calculations and the Monte Carlo models. A comparison of the p_{T} distributions of the $\gamma\gamma$ data to p_{T} distributions measured in γp and (π,K)p processes at similar invariant masses shows the relative increase of hard interactions in $\gamma\gamma$ processes due to the direct component. The transverse momentum and pseudorapidity distributions of the $\mathrm{K}^0_{\mathrm{S}}$ mesons are reasonably well reproduced by the NLO

calculations, but they are significantly underestimated by the Monte Carlo models PHOJET and PYTHIA.

Acknowledgements

We thank Janko Binnewies, Bernd Kniehl and Gustav Kramer for providing the NLO calculations and for many useful discussions.
We particularly wish to thank the SL Division for the efficient operation of the LEP accelerator at all energies and for their continuing close cooperation with our experimental group. We thank our colleagues from CEA, DAPNIA/SPP, CE-Saclay for their efforts over the years on the time-of-flight and trigger systems which we continue to use. In addition to the support staff at our own institutions we are pleased to acknowledge the
Department of Energy, USA,
National Science Foundation, USA,
Particle Physics and Astronomy Research Council, UK,
Natural Sciences and Engineering Research Council, Canada,
Israel Science Foundation, administered by the Israel Academy of Science and Humanities,
Minerva Gesellschaft,
Benoziyo Center for High Energy Physics,
Japanese Ministry of Education, Science and Culture (the Monbusho) and a grant under the Monbusho International Science Research Program,
German Israeli Bi-national Science Foundation (GIF),
Bundesministerium für Bildung, Wissenschaft, Forschung und Technologie, Germany,
National Research Council of Canada,
Research Corporation, USA,
Hungarian Foundation for Scientific Research, OTKA T-016660, T023793 and OTKA F-023259.

References

[1] OPAL Collaboration, K. Ackerstaff et al., Z. Phys. C73 (1997) 433.

[2] J. Binnewies, B.A. Kniehl and G. Kramer, Phys. Rev. D53 (1996) 6110.

[3] TASSO Collaboration, R. Brandelik et al., Phys. Lett. B107 (1981) 290.

[4] MARK II Collaboration, D. Cords et al., Phys. Lett. B302 (1993) 341.

[5] OMEGA Photon Collaboration, R.J. Apsimon et al., Z. Phys. C43 (1989) 63.

[6] TOPAZ Collaboration, R. Enomoto et al., Phys. Lett. B341 (1994) 238.

[7] OPAL Collaboration, K. Ahmet et al., Nucl. Instrum. Methods A305 (1991) 275;
O. Biebel et al., Nucl. Instrum. Methods A323 (1992) 169;
M. Hauschild et al., Nucl. Instrum. Methods A314 (1992) 74;
S. Anderson et al., Nucl. Instrum. Methods A403 (1998) 326.

[8] B.E. Anderson et al., IEEE Transactions on Nuclear Science 41 (1994) 845.

[9] For a recent discussion see: G. A. Schuler, *Improving the equivalent-photon approximation in electron-positron collisions*, CERN-TH/96-297 (hep-ph/9610406).

[10] T. Sjöstrand, Comp. Phys. Comm. 82 (1994) 74.

[11] R. Engel and J. Ranft, Phys. Rev. D54 (1996) 4244;
R. Engel, Z. Phys. C66 (1995) 203.

[12] G. A. Schuler and T. Sjöstrand, Z. Phys. C68 (1995) 607.

[13] M. Glück, E. Reya and A. Vogt, Phys. Rev. D46 (1992) 1973;
M. Glück, E. Reya and A. Vogt, Phys. Rev. D45 (1992) 3986.

[14] S. Jadach, B.F.L. Ward and Z. Was, Comp. Phys. Comm. 79 (1994) 503.

[15] S. Jadach, W. Płaczek, B.F.L. Ward, in 'Physics at LEP2', eds. G. Altarelli, T. Sjöstrand and F. Zwirner, CERN 96-01, Vol.2 (1996).

[16] J. Fujimoto et al., in "Physics at LEP2", eds. G. Altarelli, T. Sjöstrand and F. Zwirner, CERN 96-01, Vol. 2 (1996).

[17] F.A. Berends, R. Pittau and R. Kleiss, Comp. Phys. Comm. 85 (1995) 437.

[18] J.A.M. Vermaseren, Nucl. Phys. B229 (1983) 347.

[19] J. Hilgart, R. Kleiss and F. Le Diberder, Comp. Phys. Comm. 75 (1993) 191.

[20] J. Allison et al., Nucl. Instrum. Methods A317 (1992) 47.

[21] R.M. Barnett et al., Review of Particle Physics, Phys. Rev. D54 (1996) 1.

[22] OPAL Collaboration, R. Akers et al., Z. Phys. C67 (1995) 389.

[23] OPAL Collaboration, P.D. Acton et al., Z. Phys. C 59 (1993) 183;
OPAL Collaboration, R. Akers et al., Phys. Lett. B 338 (1994) 497.

[24] J. Binnewies, B.A. Kniehl and G. Kramer, Phys. Rev. D52 (1995) 497.

[25] MARK II Collaboration, H. Schellman et al, Phys. Rev. D31 (1985) 3013.

[26] ALEPH Collaboration, D. Buskulic et al, Z. Phys. C64 (1994) 361.

[27] J. Binnewies, B.A. Kniehl and G. Kramer, Phys. Rev. D53 (1996) 3573.

	$10 < W < 30$ GeV		$30 < W < 55$ GeV	
p_{T} [GeV/c]	$\langle p_{\mathrm{T}} \rangle$ [GeV/c]	$\mathrm{d}\sigma/\mathrm{d}p_{\mathrm{T}}$ [pb/GeV/c]	$\langle p_{\mathrm{T}} \rangle$ [GeV/c]	$\mathrm{d}\sigma/\mathrm{d}p_{\mathrm{T}}$ [pb/GeV/c]
0.12-0.28	0.20	$(3.11\pm0.01\pm0.24)\times10^{4}$	0.20	$(1.06\pm0.01\pm0.08)\times10^{4}$
0.28-0.44	0.36	$(2.70\pm0.01\pm0.20)\times10^{4}$	0.35	$(8.80\pm0.06\pm0.58)\times10^{3}$
0.44-0.60	0.51	$(1.60\pm0.01\pm0.10)\times10^{4}$	0.51	$(5.31\pm0.04\pm0.32)\times10^{3}$
0.60-0.80	0.69	$(8.00\pm0.06\pm0.46)\times10^{3}$	0.69	$(2.67\pm0.03\pm0.14)\times10^{3}$
0.80-1.00	0.89	$(3.38\pm0.04\pm0.17)\times10^{3}$	0.89	$(1.26\pm0.02\pm0.06)\times10^{3}$
1.00-1.20	1.09	$(1.48\pm0.02\pm0.08)\times10^{3}$	1.09	$(5.95\pm0.12\pm0.22)\times10^{2}$
1.20-1.40	1.29	$(6.64\pm0.16\pm0.40)\times10^{2}$	1.29	$(2.92\pm0.09\pm0.12)\times10^{2}$
1.40-1.60	1.49	$(3.29\pm0.11\pm0.21)\times10^{2}$	1.49	$(1.55\pm0.07\pm0.06)\times10^{2}$
1.60-1.80	1.69	$(1.75\pm0.08\pm0.11)\times10^{2}$	1.69	$(9.01\pm0.49\pm0.55)\times10^{1}$
1.80-2.00	1.89	$(1.00\pm0.06\pm0.07)\times10^{2}$	1.89	$(5.96\pm0.39\pm0.38)\times10^{1}$
2.00-2.20	2.10	$(6.04\pm0.48\pm0.37)\times10^{1}$	2.09	$(3.29\pm0.29\pm0.13)\times10^{1}$
2.20-2.40	2.30	$(4.18\pm0.39\pm0.27)\times10^{1}$	2.29	$(2.15\pm0.23\pm0.20)\times10^{1}$
2.40-2.60	2.50	$(2.06\pm0.30\pm0.08)\times10^{1}$	2.50	$(1.64\pm0.20\pm0.07)\times10^{1}$
2.60-2.80	2.68	$(2.04\pm0.31\pm0.07)\times10^{1}$	2.70	$(1.01\pm0.16\pm0.08)\times10^{1}$
2.80-3.00	2.90	$(1.12\pm0.25\pm0.05)\times10^{1}$	2.88	$(9.18\pm1.55\pm1.10)$
3.00-3.50	3.22	$(1.09\pm0.16\pm0.11)\times10^{1}$	3.21	$(4.26\pm0.65\pm0.68)$
3.50-4.00	3.71 ± 0.01	$(6.03\pm1.35\pm0.21)$	3.74 ± 0.01	$(3.58\pm0.62\pm0.32)$
4.00-5.00	4.36 ± 0.01	$(2.99\pm0.82\pm0.33)$	4.38 ± 0.02	$(1.07\pm0.25\pm0.04)$
5.00-6.00	5.55 ± 0.03	$(1.40\pm0.64\pm0.07)$	5.50 ± 0.04	$(7.12\pm2.38\pm0.44)\times10^{-1}$
6.00-8.00	–	–	6.94 ± 0.07	$(2.74\pm1.22\pm0.15)\times10^{-1}$
8.00-15.0	–	–	9.51 ± 0.32	$(1.11\pm0.73\pm0.36)\times10^{-1}$

Table 1: Differential inclusive charged hadron production cross-sections $\mathrm{d}\sigma/\mathrm{d}p_{\mathrm{T}}$ for $|\eta| < 1.5$ and in the W ranges $10 < W < 30$ GeV and $30 < W < 55$ GeV. The first error is statistical and the second is systematic. No value is given if the error on $\langle p_{\mathrm{T}} \rangle$ is less than 0.01.

	$55 < W < 125$ GeV		$10 < W < 125$ GeV	
p_{T} [GeV/c]	$\langle p_{\mathrm{T}} \rangle$ [GeV/c]	$\mathrm{d}\sigma/\mathrm{d}p_{\mathrm{T}}$ [pb/GeV/c]	$\langle p_{\mathrm{T}} \rangle$ [GeV/c]	$\mathrm{d}\sigma/\mathrm{d}p_{\mathrm{T}}$ [pb/GeV/c]
0.12-0.28	0.20	$(5.85\pm0.05\pm0.58)\times10^{3}$	0.20	$(4.78\pm0.02\pm0.38)\times10^{4}$
0.28-0.44	0.35	$(4.75\pm0.04\pm0.46)\times10^{3}$	0.36	$(4.05\pm0.01\pm0.31)\times10^{4}$
0.44-0.60	0.51	$(2.92\pm0.03\pm0.28)\times10^{3}$	0.51	$(2.42\pm0.01\pm0.17)\times10^{4}$
0.60-0.80	0.69	$(1.53\pm0.02\pm0.12)\times10^{3}$	0.69	$(1.21\pm0.01\pm0.07)\times10^{4}$
0.80-1.00	0.89	$(7.25\pm0.15\pm0.47)\times10^{2}$	0.89	$(5.33\pm0.04\pm0.27)\times10^{3}$
1.00-1.20	1.09	$(3.89\pm0.10\pm0.20)\times10^{2}$	1.09	$(2.45\pm0.03\pm0.12)\times10^{3}$
1.20-1.40	1.29	$(1.91\pm0.07\pm0.09)\times10^{2}$	1.29	$(1.14\pm0.02\pm0.06)\times10^{3}$
1.40-1.60	1.49	$(1.04\pm0.06\pm0.04)\times10^{2}$	1.49	$(5.87\pm0.13\pm0.31)\times10^{2}$
1.60-1.80	1.69	$(6.20\pm0.41\pm0.18)\times10^{1}$	1.69	$(3.28\pm0.10\pm0.19)\times10^{2}$
1.80-2.00	1.89	$(3.78\pm0.33\pm0.20)\times10^{1}$	1.89	$(2.00\pm0.08\pm0.11)\times10^{2}$
2.00-2.20	2.09	$(2.53\pm0.27\pm0.06)\times10^{1}$	2.09	$(1.20\pm0.06\pm0.06)\times10^{2}$
2.20-2.40	2.28	$(1.72\pm0.22\pm0.04)\times10^{1}$	2.29	$(8.10\pm0.49\pm0.57)\times10^{1}$
2.40-2.60	2.50	$(1.10\pm0.18\pm0.02)\times10^{1}$	2.50	$(5.00\pm0.38\pm0.20)\times10^{1}$
2.60-2.80	2.69	$(7.89\pm1.49\pm0.23)$	2.69	$(3.81\pm0.34\pm0.18)\times10^{1}$
2.80-3.00	2.92	$(5.09\pm1.15\pm0.34)$	2.90	$(2.70\pm0.29\pm0.11)\times10^{1}$
3.00-3.50	3.23	$(3.18\pm0.59\pm0.04)$	3.22	$(1.77\pm0.16\pm0.07)\times10^{1}$
3.50-4.00	3.70±0.01	$(2.07\pm0.48\pm0.10)$	3.72	$(1.16\pm0.13\pm0.04)\times10^{1}$
4.00-5.00	4.46±0.02	$(9.30\pm2.44\pm0.58)\times10^{-1}$	4.40±0.01	$(4.32\pm0.61\pm0.19)$
5.00-6.00	5.38±0.04	$(3.30\pm1.67\pm0.64)\times10^{-1}$	5.48±0.01	$(1.95\pm0.45\pm0.09)$
6.00-8.00	6.81±0.09	$(1.24\pm0.76\pm0.05)\times10^{-1}$	6.92±0.03	$(5.97\pm2.01\pm0.40)\times10^{-1}$
8.00-15.0	9.91±0.34	$(2.64\pm1.76\pm0.23)\times10^{-2}$	9.69±0.18	$(1.10\pm0.46\pm0.07)\times10^{-1}$

Table 2: Differential inclusive charged hadron production cross-sections $\mathrm{d}\sigma/\mathrm{d}p_{\mathrm{T}}$ for $|\eta| < 1.5$ and in the W range $55 < W < 125$ GeV and for all W ($10 < W < 125$ GeV). The first error is the statistical error and the second error is the systematic error. No value is given if the error on $\langle p_{\mathrm{T}} \rangle$ is less than 0.01.

	$10 < W < 30$ GeV		$30 < W < 55$ GeV	
$\|\eta\|$	$\langle\|\eta\|\rangle$	$\mathrm{d}\sigma/\mathrm{d}\|\eta\|$ [nb]	$\langle\|\eta\|\rangle$	$\mathrm{d}\sigma/\mathrm{d}\|\eta\|$ [nb]
0.00-0.30	0.15	9.91±0.06±0.70	0.15	3.27±0.03±0.20
0.30-0.60	0.45	9.98±0.06±0.71	0.45	3.33±0.03±0.19
0.60-0.90	0.75	10.05±0.06±0.71	0.75	3.41±0.03±0.19
0.90-1.20	1.05	10.01±0.06±0.71	1.05	3.43±0.03±0.20
1.20-1.50	1.35	9.54±0.06±0.67	1.35	3.33±0.03±0.19
	$55 < W < 125$ GeV		$10 < W < 125$ GeV	
$\|\eta\|$	$\langle\|\eta\|\rangle$	$\mathrm{d}\sigma/\mathrm{d}\|\eta\|$ [nb]	$\langle\|\eta\|\rangle$	$\mathrm{d}\sigma/\mathrm{d}\|\eta\|$ [nb]
0.00-0.30	0.15	1.80±0.02±0.16	0.15	14.97±0.06±1.12
0.30-0.60	0.45	1.85±0.02±0.17	0.45	15.16±0.07±1.13
0.60-0.90	0.75	1.88±0.02±0.17	0.75	15.33±0.07±1.14
0.90-1.20	1.05	1.93±0.02±0.16	1.05	15.35±0.07±1.15
1.20-1.50	1.35	1.90±0.02±0.16	1.35	14.75±0.06±1.08

Table 3: Differential inclusive charged hadron production cross-sections $\mathrm{d}\sigma/\mathrm{d}|\eta|$ for $p_{\mathrm{T}} > 120$ MeV/c and in the W ranges $10 < W < 30$ GeV, $30 < W < 55$ GeV, $55 < W < 125$ GeV and for all W ($10 < W < 125$ GeV). The first error is the statistical error and the second error is the systematic error.

	$10 < W < 30$ GeV		$30 < W < 55$ GeV	
$\|\eta\|$	$\langle\|\eta\|\rangle$	$\mathrm{d}\sigma/\mathrm{d}\|\eta\|$ [nb]	$\langle\|\eta\|\rangle$	$\mathrm{d}\sigma/\mathrm{d}\|\eta\|$ [nb]
0.00-0.30	0.15	$(8.26\pm0.47\pm0.37)\times10^{-2}$	0.14	$(4.51\pm0.27\pm0.20)\times10^{-2}$
0.30-0.60	0.45	$(9.33\pm0.49\pm0.49)\times10^{-2}$	0.45	$(4.36\pm0.27\pm0.09)\times10^{-2}$
0.60-0.90	0.75	$(7.72\pm0.45\pm0.24)\times10^{-2}$	0.76	$(4.66\pm0.28\pm0.44)\times10^{-2}$
0.90-1.20	1.05	$(7.95\pm0.47\pm0.35)\times10^{-2}$	1.05	$(4.39\pm0.29\pm0.27)\times10^{-2}$
1.20-1.50	1.34	$(8.17\pm0.47\pm0.31)\times10^{-2}$	1.35	$(4.56\pm0.30\pm0.19)\times10^{-2}$
	$55 < W < 125$ GeV		$10 < W < 125$ GeV	
$\|\eta\|$	$\langle\|\eta\|\rangle$	$\mathrm{d}\sigma/\mathrm{d}\|\eta\|$ [nb]	$\langle\|\eta\|\rangle$	$\mathrm{d}\sigma/\mathrm{d}\|\eta\|$ [nb]
0.00-0.30	0.15	$(3.07\pm0.24\pm0.07)\times10^{-2}$	0.15	$(1.62\pm0.06\pm0.09)\times10^{-1}$
0.30-0.60	0.45	$(2.91\pm0.23\pm0.09)\times10^{-2}$	0.45	$(1.65\pm0.06\pm0.08)\times10^{-1}$
0.60-0.90	0.75	$(3.21\pm0.25\pm0.07)\times10^{-2}$	0.75	$(1.59\pm0.06\pm0.09)\times10^{-1}$
0.90-1.20	1.05	$(3.14\pm0.25\pm0.12)\times10^{-2}$	1.05	$(1.55\pm0.06\pm0.07)\times10^{-1}$
1.20-1.50	1.35	$(3.35\pm0.26\pm0.07)\times10^{-2}$	1.35	$(1.60\pm0.06\pm0.07)\times10^{-1}$

Table 4: Differential inclusive charged hadron production cross-sections $\mathrm{d}\sigma/\mathrm{d}|\eta|$ for $p_{\mathrm{T}} > 1.5$ GeV/c and in the W ranges $10 < W < 30$ GeV, $30 < W < 55$ GeV, $55 < W < 125$ GeV and for all W ($10 < W < 125$ GeV). The first error is the statistical error and the second error is the systematic error.

	$10 < W < 125$ GeV	
p_{T} [GeV/c]	$\langle p_{\mathrm{T}} \rangle$ [GeV/c]	$\mathrm{d}\sigma/\mathrm{d}p_{\mathrm{T}}$ [pb/GeV/c]
1.0–1.2	1.09 ±0.01	206.2 ± 17.4 ± 16.1
1.2–1.5	1.33 ±0.01	100.2 ± 8.9 ± 8.5
1.5–1.9	1.66 ±0.01	32.9 ± 4.5 ± 3.7
1.9–2.4	2.11 ±0.02	13.5 ± 2.6 ± 1.3
2.4–3.0	2.65 ±0.04	5.2 ± 1.3 ± 0.7
3.0–4.0	3.37 ±0.08	2.0 ± 0.7 ± 0.2
4.0–5.5	4.56 ±0.15	0.4 ± 0.3 ± 0.1

Table 5: Differential inclusive $\mathrm{K}^0_{\mathrm{S}}$ production cross-sections $\mathrm{d}\sigma/\mathrm{d}p_{\mathrm{T}}$ for $p_{\mathrm{T}}(\mathrm{K}^0_{\mathrm{S}}) > 1$ GeV/c and $|\eta(\mathrm{K}^0_{\mathrm{S}})| < 1.5$ in the W range $10 < W < 125$ GeV. The first error is the statistical error and the second error is the systematic error.

$\lvert\eta\rvert$	$\langle\lvert\eta\rvert\rangle$	$\mathrm{d}\sigma/\mathrm{d}\lvert\eta\rvert$ [pb]
0.0–0.3	0.15 ± 0.01	61.7 ± 7.2 ± 5.2
0.3–0.6	0.45 ± 0.01	63.1 ± 7.3 ± 5.4
0.6–0.9	0.76 ± 0.01	72.4 ± 7.8 ± 6.1
0.9–1.2	1.05 ± 0.01	70.2 ± 8.0 ± 4.7
1.2–1.5	1.34 ± 0.01	58.0 ± 7.5 ± 4.0

Table 6: Differential inclusive $\mathrm{K}^0_{\mathrm{S}}$ production cross-sections $\mathrm{d}\sigma/\mathrm{d}|\eta|$ for $p_{\mathrm{T}}(\mathrm{K}^0_{\mathrm{S}}) > 1$ GeV/c and $|\eta(\mathrm{K}^0_{\mathrm{S}})| < 1.5$ in the W range $10 < W < 125$ GeV. The first error is the statistical error and the second error is the systematic error.

	$10 < W < 35$ GeV		$35 < W < 125$ GeV	
p_{T} [GeV/c]	$\langle p_{\mathrm{T}} \rangle$ [GeV/c]	$\mathrm{d}\sigma/\mathrm{d}p_{\mathrm{T}}$ [pb/GeV/c]	$\langle p_{\mathrm{T}} \rangle$ [GeV/c]	$\mathrm{d}\sigma/\mathrm{d}p_{\mathrm{T}}$ [pb/GeV/c]
1.0–1.2	1.08 ±0.01	127.3 ± 14.6 ± 12.6	1.10 ±0.01	75.0 ± 9.5 ± 5.1
1.2–1.5	1.33 ±0.01	73.6 ± 8.4 ± 6.6	1.33 ±0.01	30.0 ± 4.3 ± 2.3
1.5–1.9	1.66 ±0.02	19.8 ± 3.4 ± 2.5	1.67 ±0.02	13.1 ± 3.0 ± 2.3
1.9–2.4	2.11 ±0.03	9.8 ± 2.8 ± 1.3	2.11 ±0.03	4.4 ± 1.2 ± 0.4
2.4–3.0	2.72 ±0.04	1.7 ± 0.9 ± 0.2	2.62 ±0.05	2.9 ± 0.8 ± 0.6
3.0–4.0	3.37 ±0.15	0.9 ± 0.4 ± 0.3	3.38 ±0.09	1.0 ± 0.6 ± 0.2
4.0–5.5	–	–	4.56 ±0.15	0.3 ± 0.3 ± 0.1

Table 7: Differential inclusive $\mathrm{K}^0_{\mathrm{S}}$ production cross-sections $\mathrm{d}\sigma/\mathrm{d}p_{\mathrm{T}}$ for $p_{\mathrm{T}}(\mathrm{K}^0_{\mathrm{S}}) > 1$ GeV/c and $|\eta(\mathrm{K}^0_{\mathrm{S}})| < 1.5$ in the W ranges $10 < W < 35$ GeV and $35 < W < 125$ GeV. The first error is the statistical error and the second error is the systematic error.

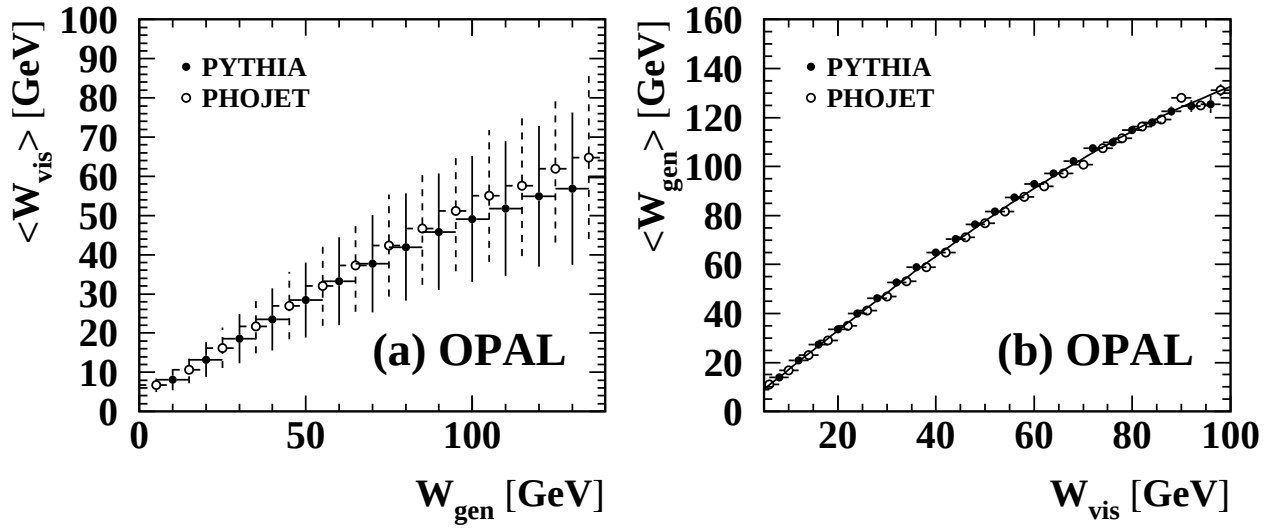

Figure 1: The relation between the generated hadronic invariant mass $W_{\rm gen}$ and the visible hadronic invariant mass $W_{\rm vis}$ for PHOJET and PYTHIA Monte Carlo events. The vertical bars show the standard deviation in each bin in (a) and the error on the mean in (b). The polynomial fit shown in (b) determines the correction function for $W_{\rm vis}$.

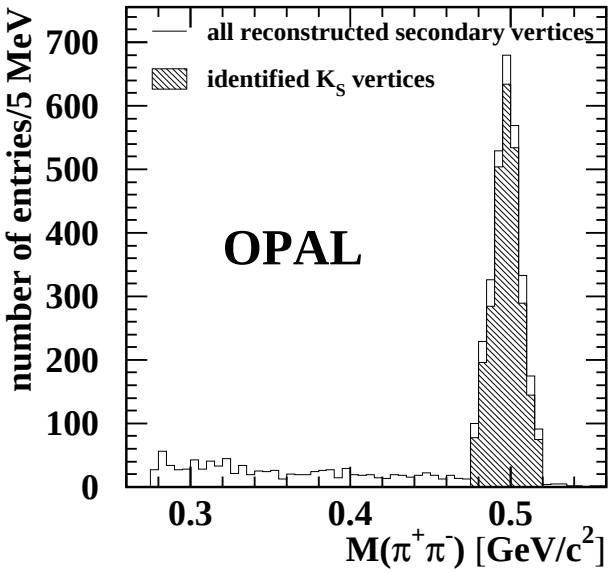

Figure 2: Distribution of the $\pi^+\pi^-$ invariant mass M for all identified secondary vertices in the selected events before (open histogram) and after (hatched histogram) applying the cut $|M(\pi^+\pi^-) - 0.4977\ \mathrm{GeV}/c^2| < 0.02\ \mathrm{GeV}/c^2$ and the $\mathrm{d}E/\mathrm{d}x$ cuts used to identify $\mathrm{K}^0_{\mathrm{S}} \to \pi^+\pi^-$ vertices.

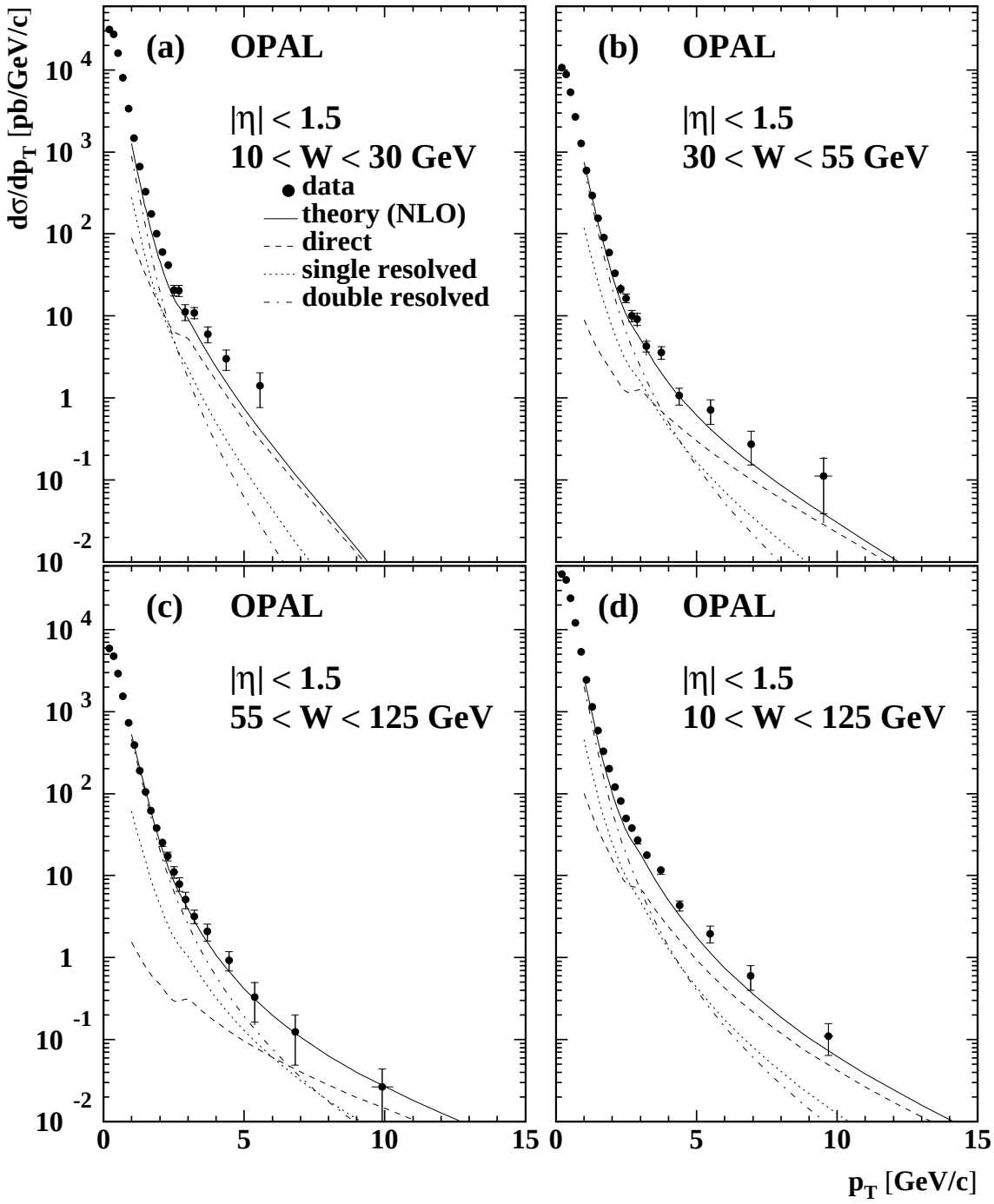

Figure 3: Differential inclusive charged hadron production cross-sections $\mathrm{d}\sigma/\mathrm{d}p_{\mathrm{T}}$ for $|\eta| < 1.5$ and in the W ranges (a) $10 < W < 30$ GeV; (b) $30 < W < 55$ GeV; (c) $55 < W < 125$ GeV and (d) for all W ($10 < W < 125$ GeV) measured at $\sqrt{s}_{\mathrm{ee}} = 161$ and 172 GeV. The data are compared to NLO calculations for $p_{\mathrm{T}} > 1$ GeV/c by Binnewies et al. together with the separate contributions of double-resolved, single-resolved and direct $\gamma\gamma$ interactions. The inner error bar shows the statistical error and the outer error bar the statistical and systematic errors added in quadrature.

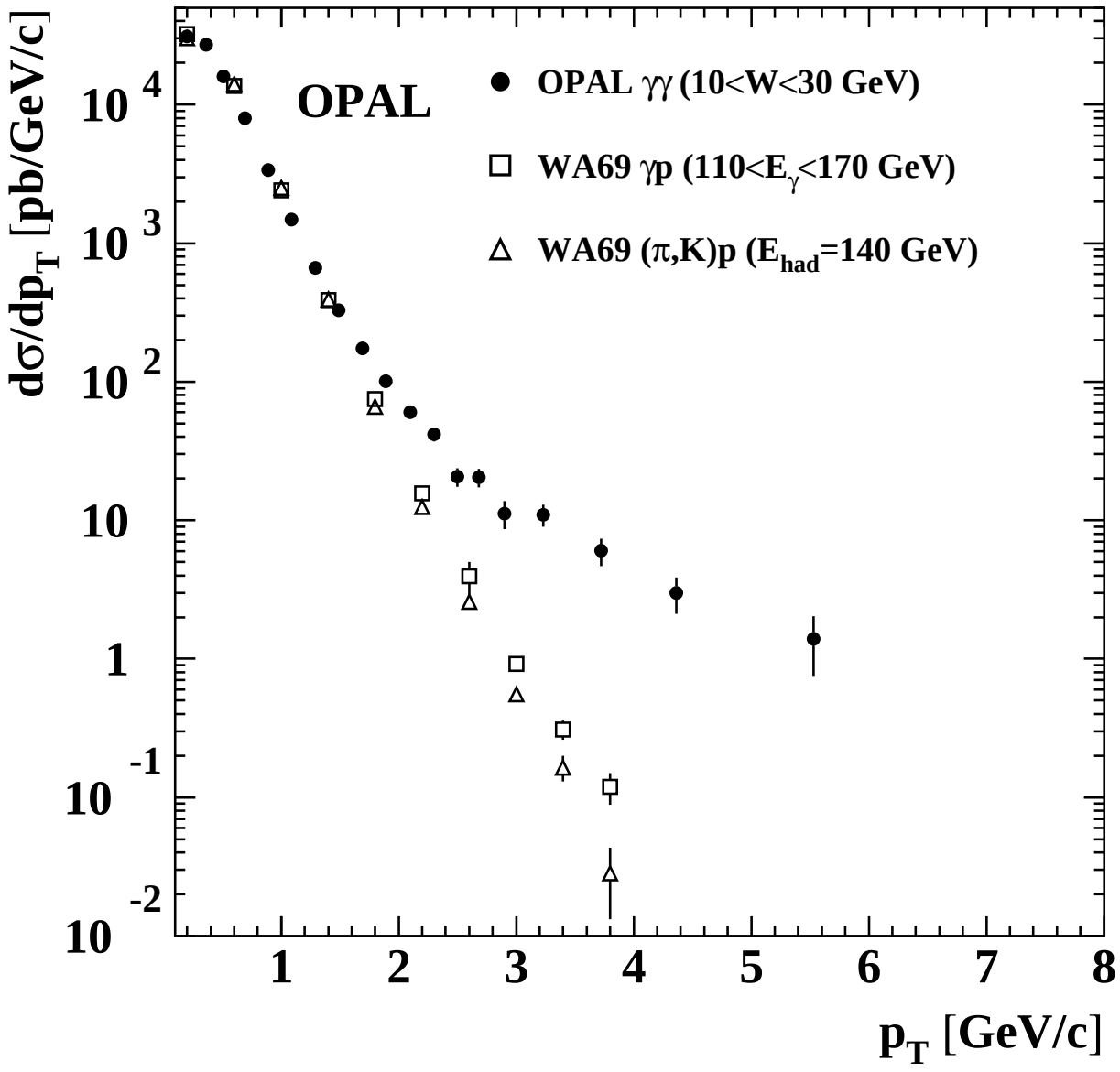

Figure 4: The p_{T} distribution measured in $\gamma\gamma$ interactions in the range $10 < W < 30$ GeV is compared to the p_{T} distribution measured in γp and hp (h= π,K) interactions in the experiment WA69 [5]. The hp and γp data are normalised to the low p_{T} region at $p_{\mathrm{T}} \approx 200$ MeV/c. The cross-section values given on the ordinate are therefore only valid for the OPAL data.

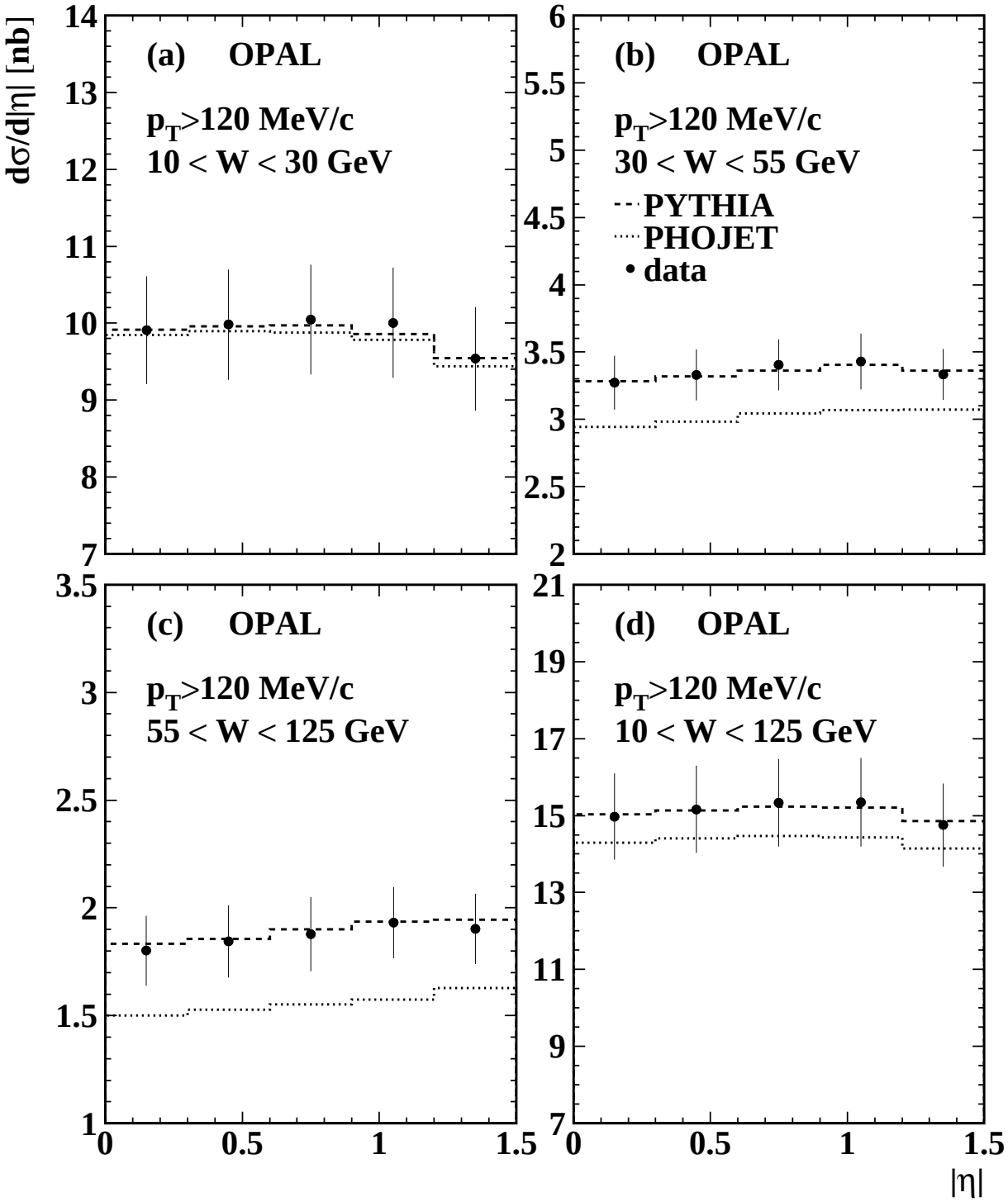

Figure 5: Differential inclusive charged hadron production cross-sections $\mathrm{d}\sigma/\mathrm{d}|\eta|$ for $p_{\mathrm{T}} > 120$ MeV/c and in the W ranges (a) $10 < W < 30$ GeV; (b) $30 < W < 55$ GeV; (c) $55 < W < 125$ GeV and (d) for all W ($10 < W < 125$ GeV) measured at $\sqrt{s}_{\mathrm{ee}} = 161$ and 172 GeV. The data are compared to the PHOJET and PYTHIA simulation. The Monte Carlo distributions are plotted as histograms using the same bin width as for the data. The statistical error is smaller than the symbol size. The error bars show the statistical and systematic errors added in quadrature.

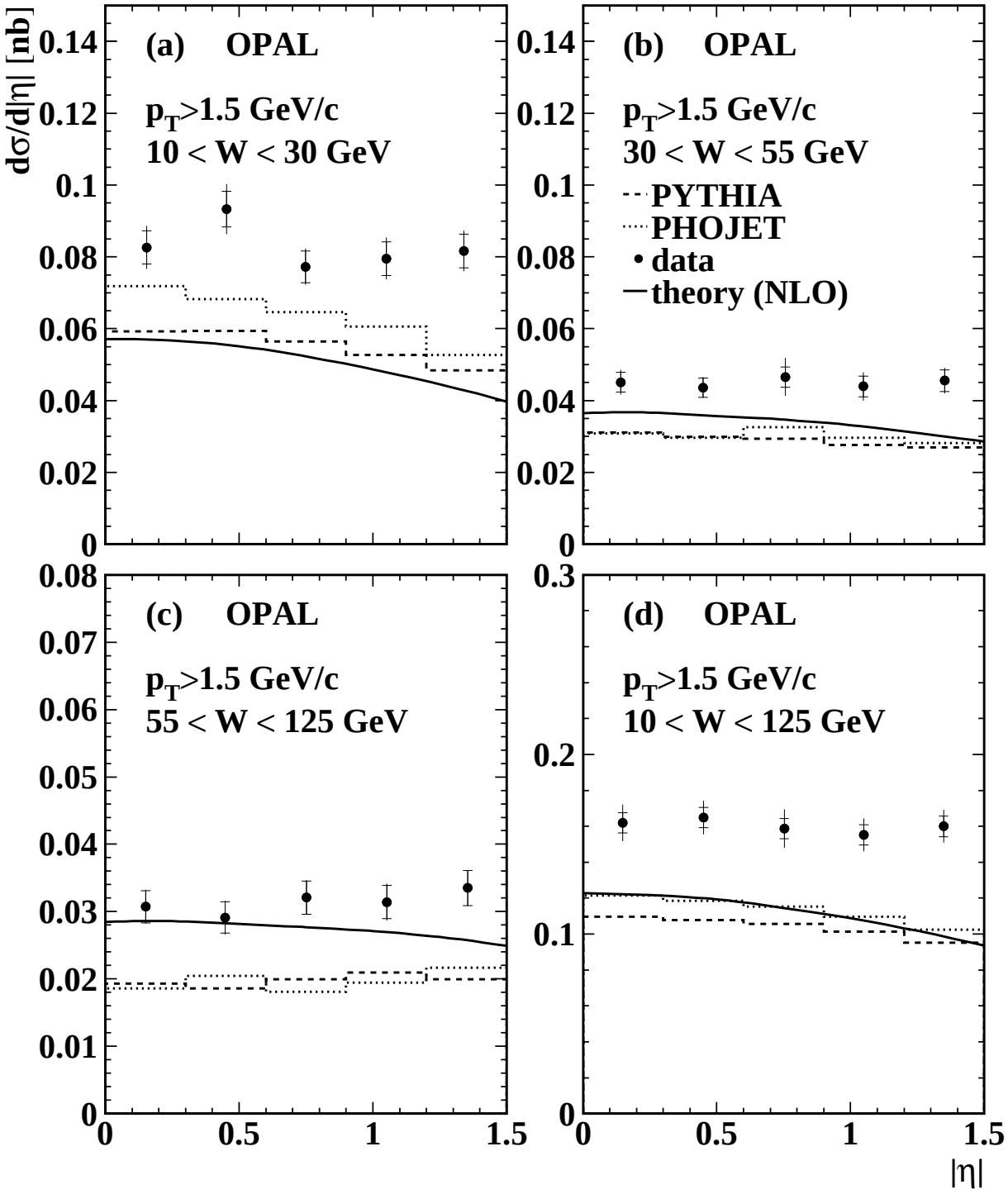

Figure 6: Differential inclusive charged hadron production cross-sections $\mathrm{d}\sigma/\mathrm{d}|\eta|$ for $p_{\mathrm{T}} > 1.5$ GeV/c and in the W ranges (a) $10 < W < 30$ GeV; (b) $30 < W < 55$ GeV; (c) $55 < W < 125$ GeV and (d) for all W ($10 < W < 125$ GeV) measured at $\sqrt{s}_{\mathrm{ee}} = 161$ and 172 GeV. The data are compared to the PHOJET and PYTHIA simulation and to NLO calculations. The Monte Carlo distributions are plotted as histograms using the same bin width as for the data. The inner error bar shows the statistical error and the outer error bar the statistical and systematic errors added in quadrature.

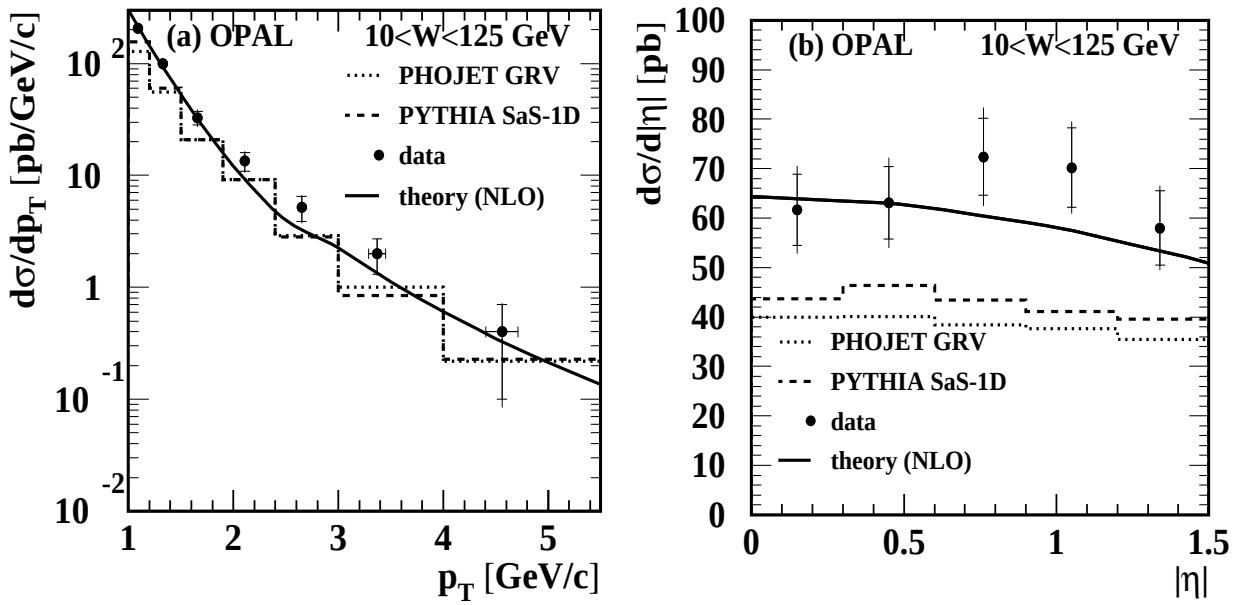

Figure 7: Differential inclusive K^0_S production cross-sections (a) $d\sigma/dp_T$ and (b) $d\sigma/d|\eta|$ for $p_T(K^0_S) > 1$ GeV/c and $|\eta(K^0_S)| < 1.5$ in the W range $10 < W < 125$ GeV. The data are compared to the PHOJET and PYTHIA simulation and to NLO calculations. The data were taken at $\sqrt{s}_{ee} = 161$ and 172 GeV. The Monte Carlo distributions are plotted as histograms using the same bin width as for the data. The inner error bar shows the statistical error and the outer error bar the statistical and systematic errors added in quadrature.

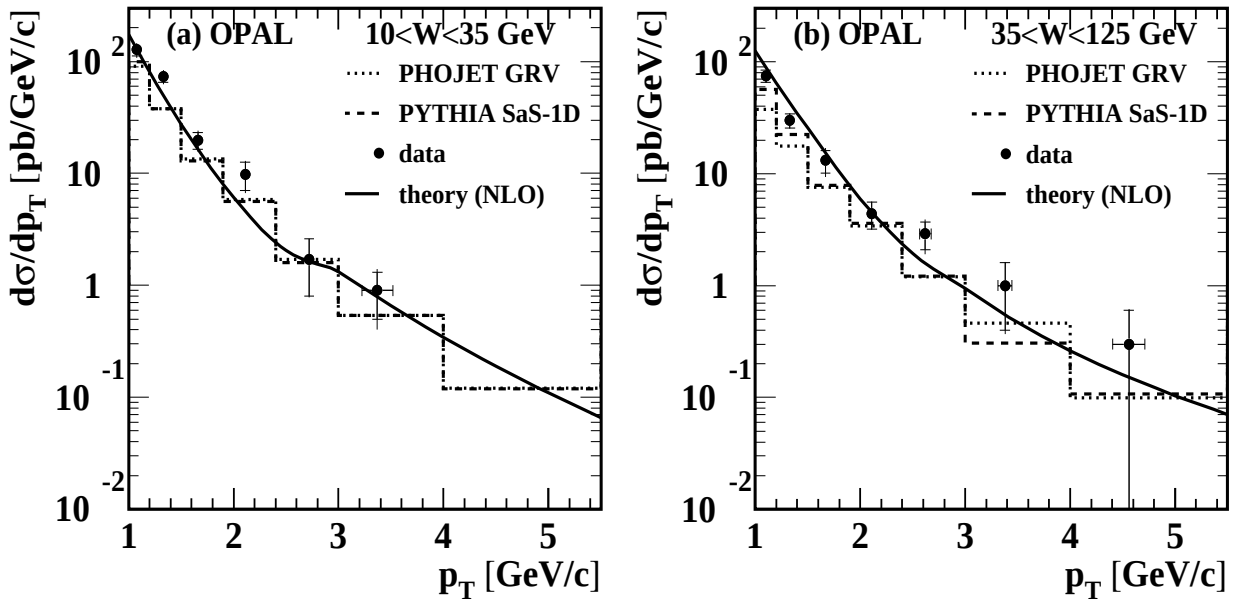

Figure 8: Differential inclusive K^0_S production cross-sections $d\sigma/dp_T$ for $p_T(K^0_S) > 1$ GeV/c and $|\eta(K^0_S)| < 1.5$ in the W ranges (a) $10 < W < 35$ GeV and (b) $35 < W < 125$ GeV. The data are compared to the PHOJET and PYTHIA simulation and to NLO calculations. The data were taken at $\sqrt{s}_{ee} = 161$ and 172 GeV. The Monte Carlo distributions are plotted as histograms using the same bin width as for the data. The inner error bar shows the statistical error and the outer error bar the statistical and systematic errors added in quadrature.